Nanoscale

PAPER

View Article Online
View Journal | View Issue

Cite this: *Nanoscale*, 2023, **15**, 11884

Interfacial engineering to modulate surface dipoles, work functions and dielectric confinement of halide perovskites†

Pooja Basera,[a,b] Boubacar Traoré,[a] Jacky Even *[b] and Claudine Katan *[a]

The interfacial properties between perovskite photoactive and charge transport layers are critical for device performance and operational stability. Therefore, an accurate theoretical description of the link between surface dipoles and work functions is of scientific and practical interest. We show that for a $CsPbBr_3$ perovskite surface functionalized by dipolar ligand molecules, the interplay between surface dipoles, charge transfers, and local strain effects leads to upward or downward shifts of the valence level. We further demonstrate that the contribution of individual molecular entities to the surface dipoles and electric susceptibilities are essentially additive. Finally, we compare our results to those predicted from conventional classical approaches based on a capacitor model that links the induced vacuum level shift and the molecular dipole moment. Our findings identify recipes to fine-tune materials work functions that provide valuable insights into the interfacial engineering of this family of semiconductors.

Received 10th March 2023,
Accepted 25th June 2023

DOI: 10.1039/d3nr01126g

rsc.li/nanoscale

Introduction

Metal halide perovskites have received remarkable attention in the scientific community because they represent a promising class of semiconductors for optoelectronics, with simple, easy and cheap fabrication processes.[1] Attractive properties, such as tunable band gap,[2] long carrier diffusion length,[3] ambipolar charge transport,[4] high defect tolerance[5] have led to various and promising applications in the field of optoelectronic devices, such as solar cells,[6] photodetectors,[7] light emitting diodes[8] and lasers.[9] It is now common knowledge that "interfaces" are central to the performances of all these devices.[10] The interface materials having an energetically favorable alignment between the photoactive layer and the charge transport layers provide efficient operation.[11] For instance, suitable alignments with hole transport layer and the electron transport layer aid to enhance the performance of solar cells by effectively transporting the charge carriers towards the electrode layers. On the other hand, proper alignment is also required to facilitate carrier injection towards the photoactive layer for LEDs. Therefore, it is of great interest in the field of surface and interface engineering to develop methods that can effectively tailor the energy levels of the materials. Nowadays, surface functionalization has already proved successful in fine tuning the energy level alignments between the various materials composing the device. Surface functionalization directly affects the surface dipoles that subsequently influence the work function or the energy levels of the material at the interface.[11,12] In this regard, the widely used method to achieve a desired interface energetics is to tune the energy levels by introducing specific molecules having significant dipole moment with the correct orientation.[13–16]

Assessment of the impact of interface functionalization on band alignment requires detailed knowledge about its nature and composition. But, a proper characterization of interfaces is challenging in thin-films because of the presence of harsh surfaces and the difficulty to control their morphologies during the fabrication process. In addition, implementation of classical characterization techniques such as Ultraviolet Photoelectron Spectroscopy (UPS) may be difficult because molecules may tend to detach in an ultra-high vacuum region.[13] Therefore, to ascertain meaningful conclusions,

---

[a] *Univ Rennes, ENSCR, CNRS, ISCR – UMR 6226, F-35000 Rennes, France. E-mail: claudine.katan@univ-rennes1.fr*

[b] *Univ Rennes, INSA Rennes, CNRS, Institut FOTON – UMR 6082, F-35000 Rennes, France. E-mail: Jacky.Even@insa-rennes.fr*

† Electronic supplementary information (ESI) available: Computational details; definition and convention; investigated ligands; convergence of carbon chain length for the molecules on a $CsPbBr_3$ surface; surface energies of CsBr and $PbBr_2$ terminated slabs; polarization density profile for phosphonate anion on a $CsPbBr_3$ surface; surface relaxation effect on valence levels; detailed results for oleate anion and DMSO molecule on a $CsPbBr_3$ surface; band structure of $CsPbBr_3$ slabs with phosphonate, oleate, DMSO, aniline, aniline $-OCH_3$ and aniline $-NO_2$ (two orientations) as well as anilinium and its derivatives; experimental valence energy positions of aniline, aniline $-OCH_3$ and aniline $-NO_2$-treated $CsPbBr_3$ reported in the literature for perovskite films; additional results on the additivity of surface dipole densities and electric susceptibilities; computed position dependent high frequency dielectric profiles and dielectric constants at the position of the molecules. See DOI: **https://doi.org/10.1039/d3nr01126g**

various experimental techniques need to be combined, such as Kelvin probe (KP), Kelvin probe force microscopy (KPFM), Ambient Pressure Photoemission Spectroscopy (APS) and cyclic voltammetry (CV).[13,17,18] Theoretical investigations taking into account the atomistic description of surfaces and interfaces may thus provide interesting guidance for experimental work and future developments.

Regarding the theoretical approaches, some empirical models have been developed in the past, targeting mainly monolayers and metal-oxides. For example, Demchak and Fort,[19] developed an empirical model to inspect monolayers at water–air interfaces, which was later on applied to explore ultrathin layers consisting of dipolar molecules and a capacitor model. More recently, Leung *et al.*[20] demonstrated the relationship between surface dipole density and work function, and its strong dependence on the substrate's orientation, along with adsorbate-induced charge transfer. Zheng *et al.*[21] used a similar approach to tune the work function of γ-$CsSnI_3$ as a function of surface dipoles and ligand layer coverage. Recently, some of us further extended the scope of such approaches with a theoretical framework that allows bridging results from atomistic *ab initio* calculations and classical simulation approaches for multilayered thin film devices.[22]

Surface functionalization and/or passivation has already been well explored experimentally for metal halide perovskites. For instance, molecules such as mercaptobenzimidazole with $-NO_2$ and $-OCH_3$ groups are employed to modify the perovskite ($CH_3NH_3PbI_{3-x}Cl_x$)/electron transport layer interface, leading to enhanced power conversion efficiency (PCE) and stability.[23] Recently, J. Duan *et al.* regulated the side group of an aniline molecule based on the same functional groups on $CsPbBr_3$ perovskite solar cells.[24] In addition, recent theoretical studies proposed phenylethylammonium (PEA^+) and its halogen derivatives ($XPEA^+$) to passivate the surface of γ-$CsSnI_3$,[21] and DMSO and (2,4,6-trimethylphenyl) phosphonic acid (TMPPA) molecules to passivate the surfaces of both $CsPbI_3$ and $MAPbI_3$ slabs.[22] Notably, the aforementioned studies mainly focused on only one kind of molecules or side group regulated dipolar passivating molecules. Hence, there are not many reports that bring a comparative discussion on the effect of various ligands and their surface coverage to fine tune the work function of the perovskites.

In this work, we further exploit the semi-classical approach recently developed by some of us to tailor the surface dipole and work function of $CsPbBr_3$.[22] This perovskite material has recently shown great promises not only for light emitting devices, such as deep blue[25] and single photon emitters,[26] but also radiation-detectors[27,28] and can be synthesized in various forms, namely single crystals,[28–30] thin films,[31] nanoplatelets,[25,32] colloidal quantum dots[33] and superlattices.[34,35] Ligands under consideration are phosphonate, oleate, DMSO, anilinium, anilinium $-NO_2$, anilinium $-OCH_3$, and three different alkylammonium ligands [primary dodecylammonium (DA), secondary didodecylammonium (DDA), and quaternary dimethyldidodecylammonium (DMDDA)]. This specific set of ligands has been chosen based on their use in the synthesis of perovskite materials and nanocrystals, either as capping ligands and/or as passivation agents.[36–40] Aniline derivatives were added given the available data on work function shifts,[24] which motivated us to further explore their charge state and orientation. We thoroughly investigate the influence of each specific ligand on the work function and discuss the microscopic origin of the induced changes in terms of surface and interface dipoles. The impact of surface coverage is inspected. Additivity of surface and interface dipoles as well as electric susceptibilities are also discussed. Finally, we compare our results to those predicted using the conventional empirical approach based on a capacitor model and emphasize its validity in the context of halide perovskites.

Results and discussion

Interplay between surface dipole density and work function

In this section, we briefly summarize the methodology that will be used to investigate the relationship between surface/interface dipoles and work functions.[20,41] The method is based on a semi classical approach (classical physics combined with density functional theory (DFT) calculations) that has been introduced in more details in a previous work.[22] Fig. S3† provides information about the various conventions used in this work.

Relation between the polarization density and the charge density. We start by inspecting the electrodynamics that relates the displacement electric field (**D**) with the polarization density (**P**).

$$\mathbf{D} = \varepsilon_0 \mathbf{E} + \mathbf{P} \tag{1}$$

By considering Gauss' law, the polarization density is related to the bound charge density (ρ_b):

$$-\nabla \cdot \mathbf{P} = \rho_b. \tag{2}$$

The surface is modeled with a perovskite slab oriented perpendicular to the *z*-axis with the layer of molecular dipoles deposited at the surface (see ESI, Fig. S3†). The interaction between surface and molecules leads to the additivity of two dipoles: (i) the intrinsic dipole of the ligands or molecules (*vide infra*) and (ii) the dipole ascribed to the interaction between the molecules and surface. The net interaction eventually leads to a shift in perovskite surface energetics. The slab structure is built in such a way that the dipole density is vanishing in the middle bulk like region of the slab ($z = z_0 = 0$, considered as the origin) while it is also vanishing in the middle of the vacuum region (at $z = \frac{c}{2}$).

We consider the planar averaged charge density along *z* ($\rho_b(z)$) concomitant with the density profile of the polarization density along the *z* axis (P_z)

$$\rho_b(z) = -\frac{dP_z}{dz} \tag{3}$$

The weighted integral of the charge density between z_0 and $\frac{c}{2}$ can be computed from a DFT simulation of the slab

$$p = \int_{z_0}^{c/2} P_b(z)\mathrm{d}z \tag{4}$$

where $P_b(z) = z\rho_b(z)$. Using integration by parts, this quantity is identified as the surface dipole density (p):

$$p = \int_{z_0}^{c/2} P_z(z)\mathrm{d}z \tag{5}$$

In order to get some insight into the various contributions close to the surface, a polarization density profile can be extracted by a partial integration of the weighted charge density $p(z) = \int_{z_0}^{z} P_b(z')\mathrm{d}z'$ (see Leung *et al.*[20]) or $P_b(z)$ can be represented directly as in the work of Traoré *et al.*[22]

Relation between surface dipole density and work function. In order to bridge our approach with the work of Leung *et al.*,[20] we use the numerical implementation of the surface dipole density (from eqn (4)) and combine it with Poisson's equation ($-\varepsilon_0 \nabla^2 V = \rho_b$), a detailed derivation is given in ref. 22, to obtain

$$\frac{p}{\varepsilon_0} = V(c/2) - V(z_0) \tag{6}$$

The work function ϕ is given by $eV(c/2) - eV(z_0)$ (Fig. S3†), leading to

$$\phi = e\frac{p}{\varepsilon_0} \tag{7}$$

It is possible in the case of DFT calculations performed on semiconductors at $T = 0$ K (ref. 22) to directly relate the work function to the energy at the top of the valence band (E_v^{abs}, Fig. S3†). Therefore eqn (7) can be written as

$$E_v^{abs} = -\phi = -e\frac{p}{\varepsilon_0} \tag{8}$$

and its variation reads

$$\Delta E_v^{abs} = -e\frac{\Delta p}{\varepsilon_0} = -1.809 \times 10^{-8}\Delta p \tag{9}$$

where E_v^{abs} in Joule (J) and p surface dipole density in C m^{-1}. This work function definition in the theoretical work by Leung *et al.*[20] allows computing the electrostatic potential step for an electron to escape the material through a dipolar surface. Notice that the experimental definition of the work function is related to the position of the Fermi level (Fig. S3†), which may depend on various aspects including the sample temperature and carrier doping (*vide infra*). Eqn (9) provides a relationship between a shift in the valence energies (ΔE_v^{abs}) and a change in surface dipole density (Δp). Therefore, from the aforementioned methodology, the change in surface properties due to surface functionalization *via* dipolar molecules can be discussed using the polarization density profiles. In our work, we further validate the robustness of the DFT based methodology by comparing the ΔE_v^{abs} computed directly from the change of surface dipole density (Δp) (from eqn (9)) to the shift in the valence energies determined from the variations of the Hartree potential alignments (ΔE_v^{abs}) (for definition, see Fig. S3(d) and ESI text I.4†).

Investigated ligands

Fig. 1 shows various ligands or molecules that have been considered in this work. The names of the following are 5-carbon chain phosphonic acid (pentylphosphonic acid ($C_5H_{13}O_3P$)), 5-carbon chain oleic acid (pentanoic acid), commonly known as valeric acid ($C_5H_{10}O_2$), dimethyl sulfoxide (DMSO) ($(CH_3)_2SO$), aniline ($C_6H_5NH_2$) and its derivatives such as *p*-nitroaniline (aniline –NO_2 ($C_6H_6N_2O_2$)), *p*-methoxyaniline or *p*-anisidine (C_5H_9NO) (aniline –OCH_3).

Note that for Pentanoic acid and Pentylphosphonic acid, we consider their conjugate base *i.e.* Pentanoate ($C_5H_9O_2^-$) and Hydrogen phosphonate ($C_5H_{12}O_3P^-$). For aniline, nitroaniline, and methoxyaniline (see ESI, Fig. S4†), the corresponding conjugate acids are anilinium ($C_6H_5NH_3^+$), methoxyanilinium ($C_5H_{10}NO^+$) and nitroanilinium ($C_6H_7N_2O_2^+$). For the sake of simplicity, we refer to the considered molecules as phosphonate, oleate, DMSO, anilinium, anilinium –OCH_3 and anilinium –NO_2.

In addition, we consider three different alkylammonium ligands *i.e.* primary dodecylammonium (DA), secondary didodecylammonium (DDA), and quaternary dimethyldidodecylammonium (DMDDA). Note that, these ligands are taken from equilibrated snapshots of classical molecular dynamics (MD) simulations, so that dynamic effects are reflected in the alkyl chain of the molecules.[42]

As a first step, the distribution of charges in the molecules is shown *via* Hirshfeld charge analysis. The red (blue) region corresponds to a more negative charge (more positive charge) (see Fig. 1). Convention used for the dipole moment direction is from negative to positive charge (Fig. S3(a)†). We calculate the dipole moments of the optimized molecular structures. See Table 1 for a comparison with available experimental or theoretical data from the literature.

Molecules such as phosphonate, oleate, and DMSO act as Lewis bases (electron donating), while anilinium and its derivatives act as Lewis acids with a tendency to withdraw electrons. It is worth noting that there is a relation between the electron-withdrawing/donating nature of molecules and the shift in valence levels. Lewis acid/base interactions with the surface involve charge transfer, *i.e.* directly associated with the surface dipole density, which can be quantified using eqn (3)–(5). The surface dipole density, in turn, has an impact on the valence energy, as described by eqn (8) and (9).

Among all molecules, aniline –NO_2 presents the strongest dipole. The dipole moment of the charged molecules such as DA, DDA and DMDDA, with respect to their center of mass as the origin, are calculated as 25.45 D, 19.84 D and 16.84 D, respectively. These values are consistent with the trend obtained for amines in the literature.[47] Notably, values of charged molecules are origin dependent.

Surface–ligand interaction to tune surface dipole density and work function

Firstly, we test the robustness of our methodology by inspecting slabs of $CsPbBr_3$ without functionalization of the surfaces.

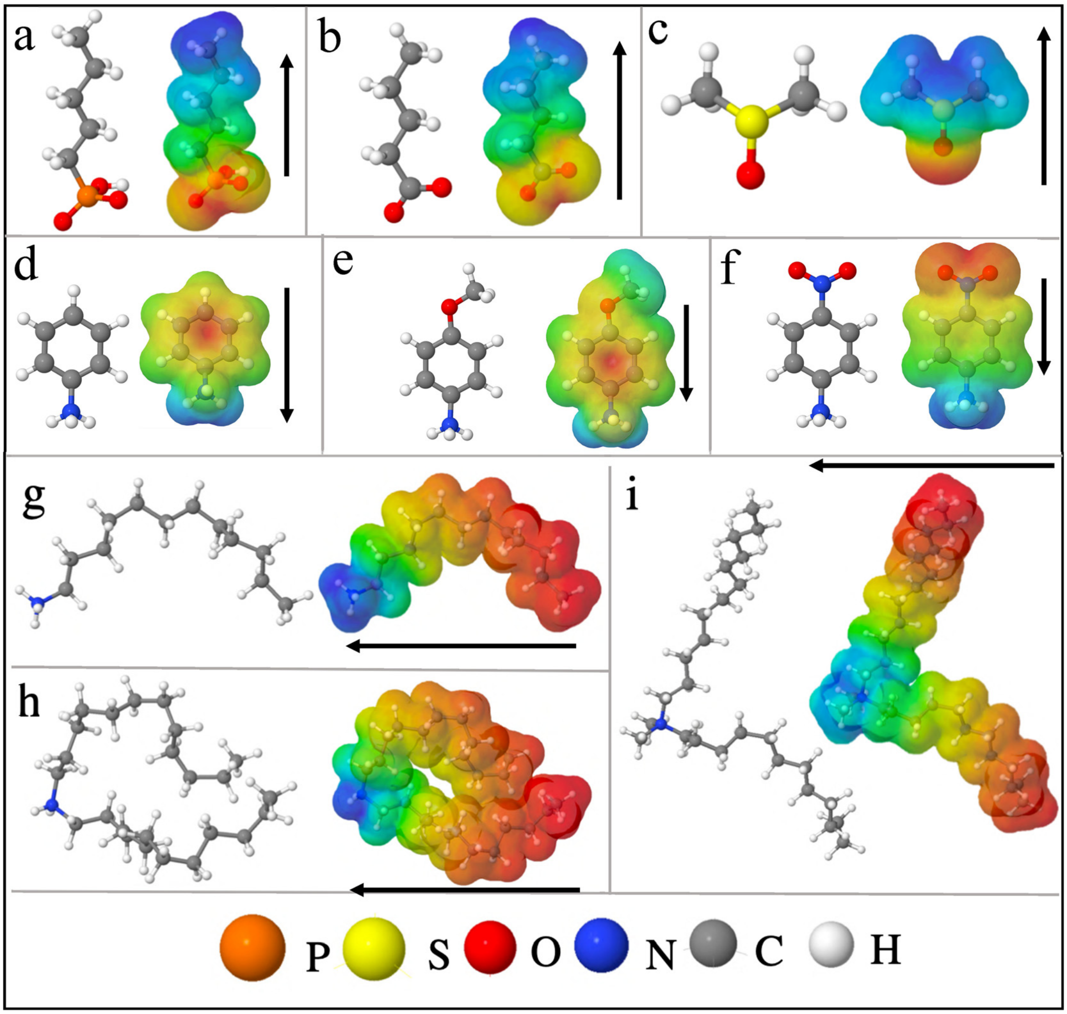

Fig. 1 Molecules and their Hirshfeld charge analysis to show the direction of the dipole moment (a) phosphonate (b) oleate (c) DMSO (d) anilinium (e) anilinium $-OCH_3$ (f) anilinium $-NO_2$. Alkylammonium ligands are taken from classical MD simulation snapshots of ref. 42: (g) primary dodecylammonium (DA) (h) secondary didodecylammonium (DDA), and (i) quaternary dimethyldidodecylammonium (DMDDA). The Red (blue) region corresponds to excess electronic charge (electron deficiency). Black arrows show the direction of the dipole moments (see Fig. S3† for sign convention).

Table 1 Computed molecular dipole moments (PBE) compared to previous works. Subscript e and t correspond to experimental and theoretical reported values

Molecules	μ (D) (calculated)	μ (D) (previous works)
Phosphonic acid	1.40	1.56_e (ref. 43)
Oleic acid	1.59	1.50_e (ref. 44)–1.61_e (ref. 45)
DMSO	3.79	3.90_e (ref. 46)
Aniline	1.70	1.97_t (ref. 24)
Aniline $-NO_2$	7.44	7.56_t (ref. 24)
Aniline $-OCH_3$	1.61	1.38_t (ref. 24)

We construct a $CsPbBr_3$ slab from its pseudo-cubic structure[27] so as to avoid issues related to symmetry breaking (see ESI for detailed discussion, Fig. S1c†). We consider the CsBr terminated surface, which appears to be more stable as compared to $PbBr_2$ terminated one.[48] We confirm this by comparing the surface energies of the CsBr and $PbBr_2$ terminated surfaces (see ESI, section V†).

Thus, we mainly proceed with the CsBr terminated surface of $CsPbBr_3$, considering a slab having 8 octahedra layers (for convergence see ESI, section I†) to study the effect of surface functionalization. To compare various approaches for the work function shifts, charge density, polarization density profiles, surface dipole densities and Hartree potential alignments are computed.

Negative surface dipole variation by surface functionalization. In many reports, molecules are shown to functionalize the surface by coordinating to lead, ascribed to the commonly observed halide vacancies in experiments.[49,50] For that purpose, phosphonic acid ligand is chosen as a good example,[39,51,52] as it is already known for its strong binding with metal ions, such as Pb in PbSe quantum dots.[53] Consistently with previously reported modeling strategies,[51,54] we remove a H atom from the phosphonic molecule (–OH end) and form a phosphonate anion. Then, we substitute a bromine (Br) atom (outer terminal) by the oxygen atom (O) of the phosphonate anion. This ensures the charge neutrality of the whole system. Note that, the pristine surface of the considered slab being terminated by four Br atoms, the concentration values of 25%, 50%, 75% and 100% correspond to substitutions of 1 Br, 2 Br, 3 Br and 4 Br atoms with phosphonate anions, respectively. The optimized structures of the pristine CsBr terminated $CsPbBr_3$ slab and that with phosphonate molecules attached to the slab are shown in Fig. 2(a). The latter is illustrated for a molecular coverage of 50%. The shaded portion shows the outer layers that are relaxed in our methodology and the middle layers are kept fixed such that they mimic the structure of bulk $CsPbBr_3$ Fig. 2(a). A computation of the Hartree potential profile can be used to analyze the valence energy of a pristine $CsPbBr_3$ slab (Fig. S3(d)†). We observe a successive increase in the valence energies (E_v^{abs}) or an upward shift of the valence levels (see Fig. 2(b)) with increasing molecular coverage. The corresponding values are summarized in Table 2.

To understand the microscopic origin of these shifts, we compute their polarization density profiles ($P_b(z)$) shown in Fig. 2(c) and analyze the surface and interface dipoles. There are few worthy points that can be highlighted from these polarization profiles ($P_b(z)$): (i) the surface dipoles counteract each other on both sides of the structure as expected from the symmetry of the slab, (ii) the dipole vanishes in the middle of the slab, (iii) by integrating the area under the peaks of the profiles ($P_b(z)$) from the center of the slab to the middle of the vacuum (eqn (5)), the surface dipole density (p) can be determined. The computed values of surface dipole densities and the change in surface dipole densities (Δp) for different concentrations (0–100%) are given in Table 2. From Fig. 2, we attribute the increase of E_v^{abs} for phosphonate to the decrease in surface dipole density induced by surface functionalization. The decrease in surface dipole density can be further explained as a result of electron transfer from the phosphonate to the outer perovskite layer, yielding a dipole direction away from the surface (see Fig. 2(d)). We examine this in more depth by looking into the interplay of octahedral tilting in the surface layer and contraction or expansion of PbBr bond lengths at the surface (see ESI, section VII†). We observe from Table S5† that when we compare 25% concentration to other concentrations (50%, 75% and 100%), the surface layers are more distorted with smaller in-plane Pb–Br–Pb angles and much larger out of plane delta (δ (ref. 55)) octahedra tilt angles. It is well known that octahedral tilting significantly influence the electronic properties.[56,57] Larger deviations from 180° in Pb–Br–Pb bond angle result in deeper valence levels. This indicates that surface relaxation addtionally impacts the dipole density at the surface, which in turn influence the

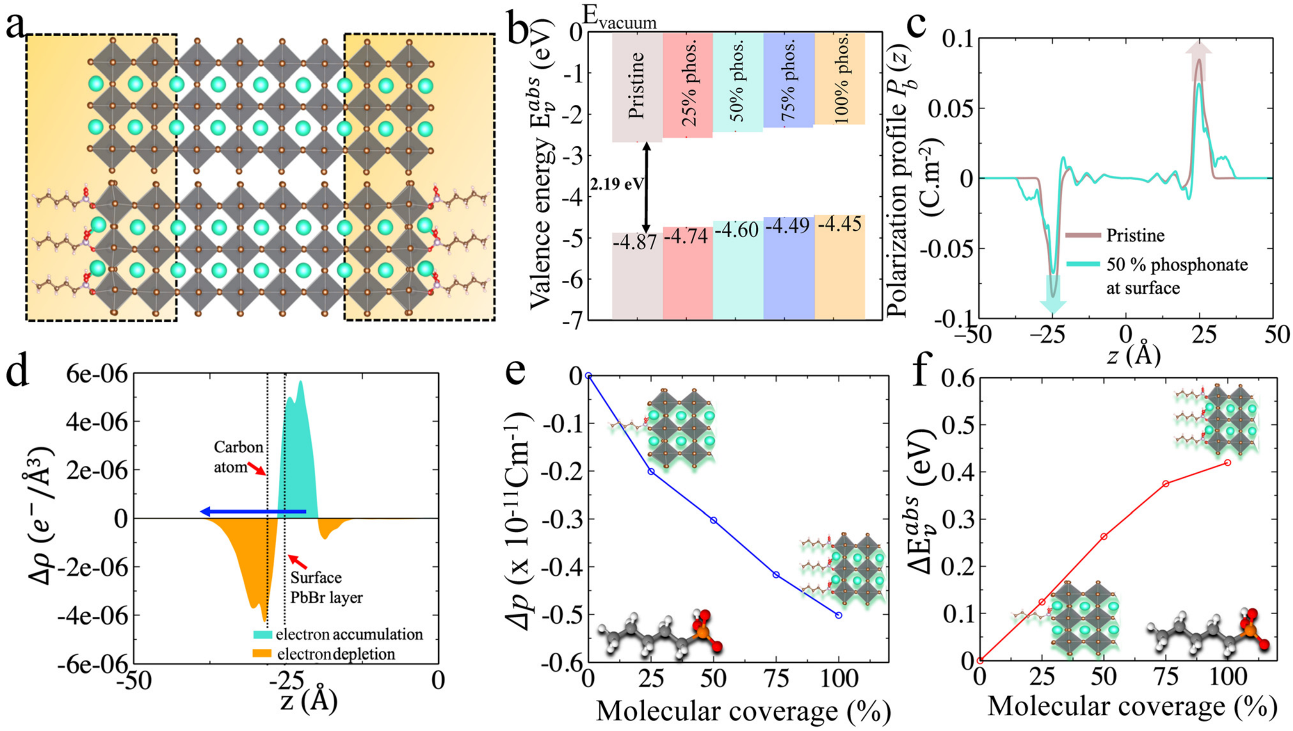

Fig. 2 (a) $CsPbBr_3$ CsBr terminated slabs without (top) and with (bottom) phosphonate ligands attached to the surface. The later is illustrated for 50% molecular coverage. (b) Valence energies for 0% to 100% surface coverage. (c) Polarization density profiles for 0% and 50% molecular coverage (for other concentrations see ESI, Fig. S7†). The integration of these polarization profiles result in the surface dipole densities (Table 2). (d) Variation of the electronic charge density upon functionalization with phosphonate for 50% molecular coverage. For clarity, only one side of the symmetric slab is shown. Orange and turquoise color represent electronic depletion and accumulation region, respectively, and the arrow indicates the net dipole direction. (e) Relation between the change in surface dipole density and the molecular coverage. (f) Relation between the change in the valence energies and the molecular coverage. The valence energy values are computed from the Hartree potential profiles.

Table 2 Valence energies (E_v^{abs}) and surface dipole densities (p) computed at the PBE + SOC level of theory for different molecules and molecular coverage changing from 0% to 100% for CsBr terminated $CsPbBr_3$ slabs. Change in surface dipole densities (Δp). Shifts of valence levels obtained from the difference of surface dipole density (ΔE_v^{abs} using eqn (9)) and computed from the Hartree potential alignment [HP] ΔE_v^{abs} (Fig. S3(d)†)

	E_v^{abs} (eV)	ΔE_v^{abs} [HP] (eV)	$p \times 10^{-11}$ (C m^{-1})	$\Delta p \times 10^{-11}$ (C m^{-1})	ΔE_v^{abs} (eV) [eqn (9)]
$CsPbBr_3$ slab with phosphonate concentration					
Pristine	−4.87	—	+3.50	—	—
25% phosphonate	−4.73	+0.14	+3.30	−0.20	+0.23
50% phosphonate	−4.60	+0.27	+3.20	−0.30	+0.34
75% phosphonate	−4.49	+0.38	+3.08	−0.42	+0.47
100% phosphonate	−4.45	+0.42	+3.00	−0.50	+0.56
$CsPbBr_3$ slab with oleate concentration					
Pristine	−4.87	—	+3.50	—	—
25% oleate	−4.63	+0.24	+3.20	−0.30	+0.34
50% oleate	−4.37	+0.50	+2.96	−0.54	+0.61
75% oleate	−4.20	+0.67	+2.83	−0.67	+0.76
100% oleate	−4.16	+0.71	+2.77	−0.73	+0.83
$CsPbBr_3$ slab with DMSO concentration					
Pristine	−4.87	—	+3.50	—	—
25% DMSO	−4.52	+0.35	+3.14	−0.36	+0.41
50% DMSO	−4.14	+0.73	+2.80	−0.70	+0.79
75% DMSO	−3.82	+1.05	+2.53	−0.97	+1.10
100% DMSO	−3.31	+1.56	+2.07	−1.43	+1.62

valence energy. Our conclusion from the aforesaid discussion is that by varying the surface coverage with phosphonate, the work function can be tuned by several meVs with a valence level shifted upwards with increasing coverage.

Next, we extend our discussion to the oleic acid and DMSO molecules, generally used as a surfactant to fabricate colloidal quantum dots.[58–60] The details regarding how these molecules are attached on the surface[50] are given in ESI (section VIII†). The calculated E_v^{abs} and surface dipole density values for various concentrations are given in Table 2. The increase in E_v^{abs} or upward shift in valence level for oleate anions and DMSO are induced by the reduction of surface dipole density as a result of charge transfer from the molecule to the outer perovskite layer (see ESI, section VIII†). Between 75% and 100% concentration of phosphonate and oleate anions, there is only a minor change in the E_v^{abs} values (~0.04 eV). It is due to the steric hindrance of bulky molecules (phosphonate and oleate) that impedes the relaxation of the surface (ESI, section VII†), which is not observed with DMSO. For lower surface coverages, the changes in surface dipole density (Δp) and the shift in the valence energies (ΔE_v^{abs}) as a function of molecular coverage for phosphonate anions are linear (see Fig. 2(e) and (f)). The linearity relationship also holds for oleate anions and DMSO (ESI, Fig. S12†). Noteworthy, the ΔE_v^{abs} obtained from Hartree potential alignment are in agreement with ΔE_v^{abs} computed using eqn (9) (see Table 2).

To sum up the aforementioned results, all the studied cases show an upwards shift of the valence level with an increase in the concentration of molecules on the surface. The observed trend is DMSO > oleate > phosphonate in effectively tuning the E_v^{abs} energies. These molecules may also act as potential passivating agents as they do not present any molecular states in between their perovskite-based band edges (ESI, Fig. S13†).

Limitation of the computational methodology. Choy and collaborators have reported their work based on mercaptobenzimidazole interface molecules and demonstrated that the defect passivation (halide vacancies) as well as tuning of energy levels can be achieved *via* modulating the functional groups, such as nitryl ($-NO_2$) and methoxyl ($-OCH_3$) groups.[23] Notably, these groups have opposite effects on the solar cell performance, owing to their different electronegativities. $-NO_2$ and $-OCH_3$ functional groups act as electron withdrawing and electron donating groups, respectively. Recently J. Duan *et al.*[24] have performed experimental studies by regulating the side group of an aniline molecule based on the same functional groups. Following this, we compute the valence energies and surface dipole densities as a function of molecular coverage for the cations on a $CsPbBr_3$ surface, and discuss our results in light of the available experimental data.[24] We first consider anilinium and its derivatives, where the $-NH_3^+$ group substitutes a Cs-atom of the outer layer of the $CsPbBr_3$ surface (Fig. 3a). At a given concentration, (Fig. 3(c) in a horizontal direction) the following trend for E_v^{abs} is observed: anilinium $-NO_2$ < anilinium < anilinium $-OCH_3$. This trend does not match the experimental trend reported for the valence bands derived from UPS spectra analysis[24] (see Fig. 3(b) and ESI, Fig. S15†). The comparison is not improved when considering neutral molecules with NH_2 group pointing towards the surface (ESI section XII†), as assumed in the original report.[24] Interestingly, with the NO_2 group pointing towards the perovskite surface (ESI section XIII†), the valence levels undergoes an upward shift. But, at the smallest computed coverage (25%), this shift is predicted to be huge, whereas the experimental one is about 0.1 eV.[24] Actually, experiments evidence a sizeable shift of the Fermi level with respect to the vacuum that points towards a *p*-doped semiconductor. This effect is not captured

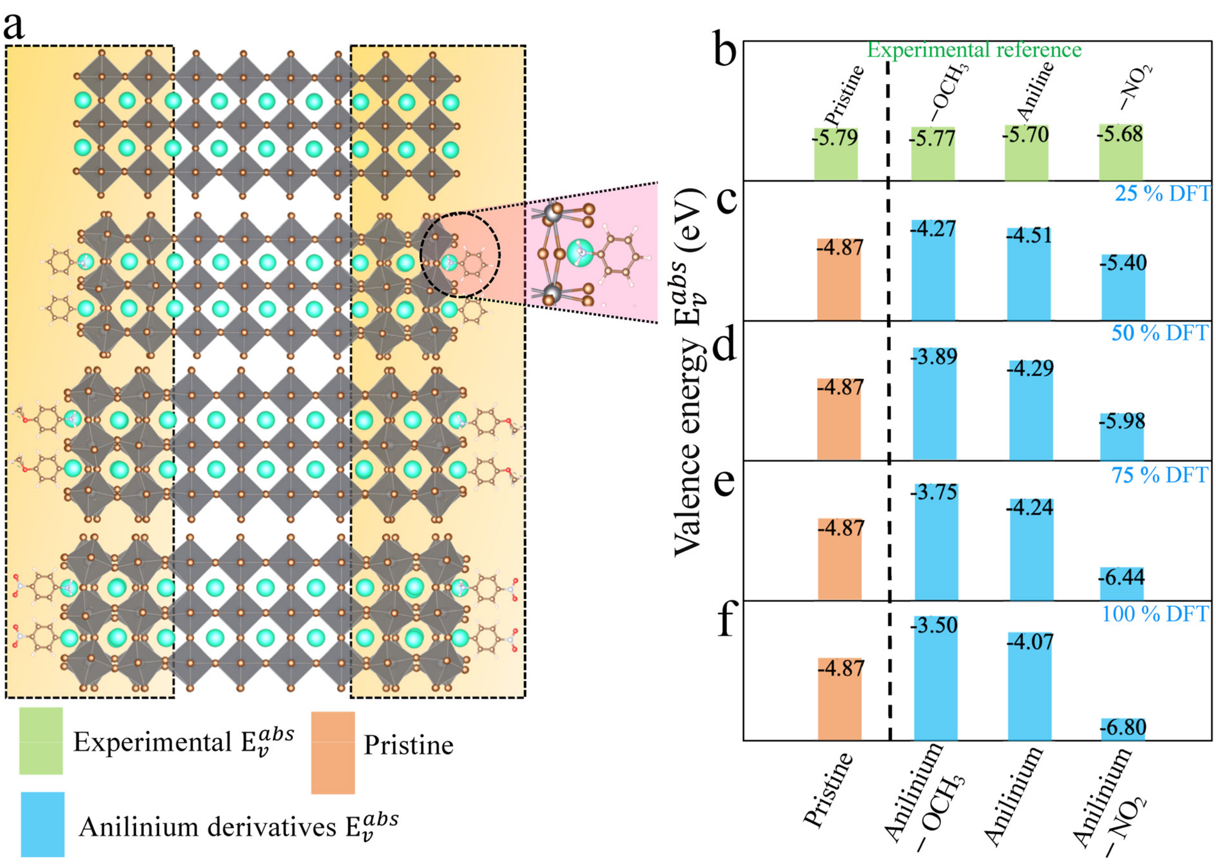

Fig. 3 (a) $CsPbBr_3$ CsBr terminated slabs without (top) and with anilinium, anilinium $-OCH_3$ and anilinium $-NO_2$ ligands on the surface. The NH_3^+ group is placed at a Cs-vacancy of the outer layers on each side of the surface (see zoom view) and is illustrated for 50% molecular coverage. (b) Experimental valence energies (top, green)[24] and (c–f) computed E_v^{abs} for pristine (orange) and for (c) 25%, (d) 50%, (e) 75%, and (f) 100% surface coverage (blue).

by the present simulations. Besides, from the computed band structures of anilinium derivatives (ESI, Fig. S14†), no in-gap molecular states are found, which confirms that they may act as potential passivating agents.

Comparison between primary, secondary and quaternary alkylammonium ligands

Recently alkylammonium ligands, particularly DMDDA halides, have attracted considerable interest in obtaining purifiable and stable colloids.[40,61,62] In light of this, we applied the present methodology to a comparison between three different alkylammonium ligands namely DA, DDA and DMDDA. We have used extracted orientations of long alkyl chain of ligands from classical MD simulations.[42] Notably, solid-state NMR spectroscopy confirmed that $CsPbBr_3$ QDs are CsBr terminated with alkylammonium ligands, partially substituting Cs cations at the surface.[63] Thus, we substitute Cs^+ with the alkylammonium ligand, replacing the cesium by the nitrogen of NH_3^+, NH_2^+ and N^+ groups corresponding to DA, DDA and DMDDA molecules, respectively (Fig. 4(a)). The computed E_v^{abs} values for DA, DDA and DMDDA are given in Table 3. As previously demonstrated, the observed trend is related to the change in surface dipole density values (Δp) obtained by integrating the area under the peak of ($P_b(z)$) shown in Fig. 4(c). We obtain small differences between the three alkylammonium ligands, including small structural distorsions of the octahedra at the surface (Table S9†). Still, experimental values may change more significantly, depending on various aspects such as surface doping, molecular coverage, molecular orientations and induced lattice strain at the surface.

Additivity of surface dipole densities and electric susceptibilities

Hitherto, we have investigated different ligands on the $CsPbBr_3$ surface, resulting in positive or negative surface dipole density variations. The increase/decrease in the valence energies is directly linked to the dipole density of the individual components comprising the whole structure.[22] Hence, it is interesting to disentangle the individual role of each entity at the interface. We illustrate this decomposition by considering two cases (i) DMSO and (ii) Aniline $-NO_2$ on a CsBr terminated $CsPbBr_3$ surface. Fig. 5(a) and (b) present

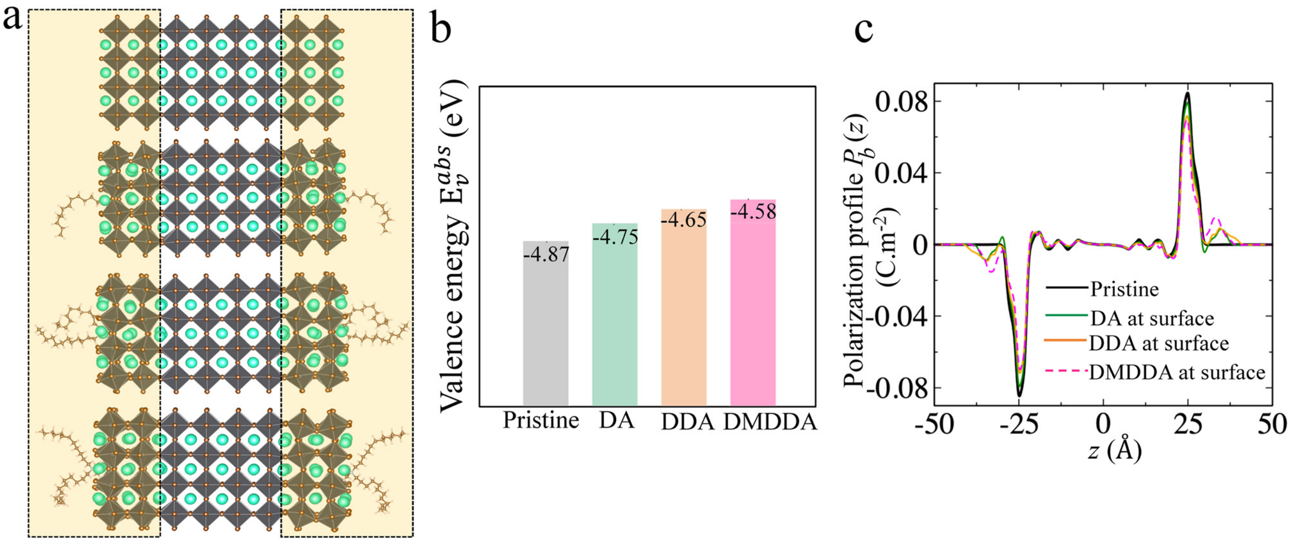

Fig. 4 (a) $CsPbBr_3$ CsBr terminated slabs without (top) and with DA, DDA and DMDDA ligands on the surface for a coverage of 11%. Corresponding (b) valence energies and (c) polarization density profiles.

Table 3 Valence energies (E_v^{abs}) and change in surface dipole densities (Δp) computed at the PBE + SOC level of theory for DA, DDA and DMDDA at CsBr terminated $CsPbBr_3$ slabs. Shifts of valence levels obtained from the difference of surface dipole density (ΔE_v^{abs} using eqn (9)) and computed from the Hartree potential alignment [HP] ΔE_v^{abs} (Fig. S3(d)†)

	E_v^{abs} (eV)	ΔE_v^{abs} [HP] (eV)	$\Delta p \times 10^{-11}$ (C m^{-1})	ΔE_v^{abs} (eV) [eqn (9)]
Pristine	−4.87	—	—	—
DA	−4.75	+0.12	−0.18	+0.20
DDA	−4.65	+0.22	−0.25	+0.28
DMDDA	−4.58	+0.29	−0.32	+0.36

the polarization density profiles ($P_b(z)$) of one side of the symmetric slab computed for the pristine perovskite (CsBr slab), the distorted pristine (distortion in the outer layer of the slab due to Cs vacancies), the isolated molecule, and the whole structure. The addition of $P_b(z)$ profiles of the distorted pristine (top panel) and the isolated molecule (middle panel) reproduce the $P_b(z)$ profile of the whole structure (bottom panel). From these $P_b(z)$ profiles, we notice that at the interface, the DMSO molecule counteracts the pristine perovskite (Fig. 5(a)), resulting in a net reduction of the surface dipole density, that subsequently lowers the work function, leading to the upwards shift of the valence level. On the contrary, aniline $-NO_2$ molecule (anilinium $-NO_2$ is shown in ESI, Fig. S20(a)†) allows to significantly increase the surface dipole density (Fig. 5(b)), with an opposite effect on the valence energy and work function.

Fig. 5(a) and (b) present the polarization density profiles ($P_b(z)$) of one side of the symmetric slab computed for the pristine perovskite (CsBr slab), the distorted pristine (distortion in the outer layer of the slab due to Cs vacancies), the isolated molecule, and the whole structure. The addition of $P_b(z)$ profiles of the distorted pristine (top panel) and the isolated molecule (middle panel) reproduce the $P_b(z)$ profile of the whole structure (bottom panel). From these $P_b(z)$ profiles, we notice that at the interface, the DMSO molecule counteracts the pristine perovskite (Fig. 5(a)), resulting in a net reduction of the surface dipole density, that subsequently lowers the work function, leading to the upwards shift of the valence level. On the contrary, aniline $-NO_2$ molecule (anilinium $-NO_2$ is shown in ESI, Fig. S20(a)†) allows to significantly increase the surface dipole density (Fig. 5(b)), with an opposite effect on the valence energy and work function.

We may inspect also the different contributions to the dielectric constant profile. Notably, the interfacial contribution to the dielectric constant profile has already been investigated in the literature using state-of-the-art first-principles approaches.[64–66] We use the same method to also show the additivity of the contributions to the electric susceptibility at the surface functionalized by molecular ligands. For that purpose, we compute the position dependent high frequency dielectric profile along the stacking axis (z) for aniline $-NO_2$ and DMSO (see ESI, Fig. S20(b)†) attached on the perovskite surface. Generally, organic molecules have a smaller dielectric constant than the inorganic perovskites. Here, we notice that the bulk dielectric constant *i.e.* 4.70, in fair agreement with earlier work,[49] is nicely captured at the center of the pristine slab. The variation in from $\varepsilon_{r1} = 4.70$ at the center of the dielectric constant profile (pristine distorted) to $\varepsilon_{r2} = 1.32$ (at the position of the isolated molecule) illustrates the presence of dielectric confinement effects (see Fig. 5(c), bottom panel). The dielectric constant profiles of the whole structures (bottom panel) are reasonably well decomposed into their

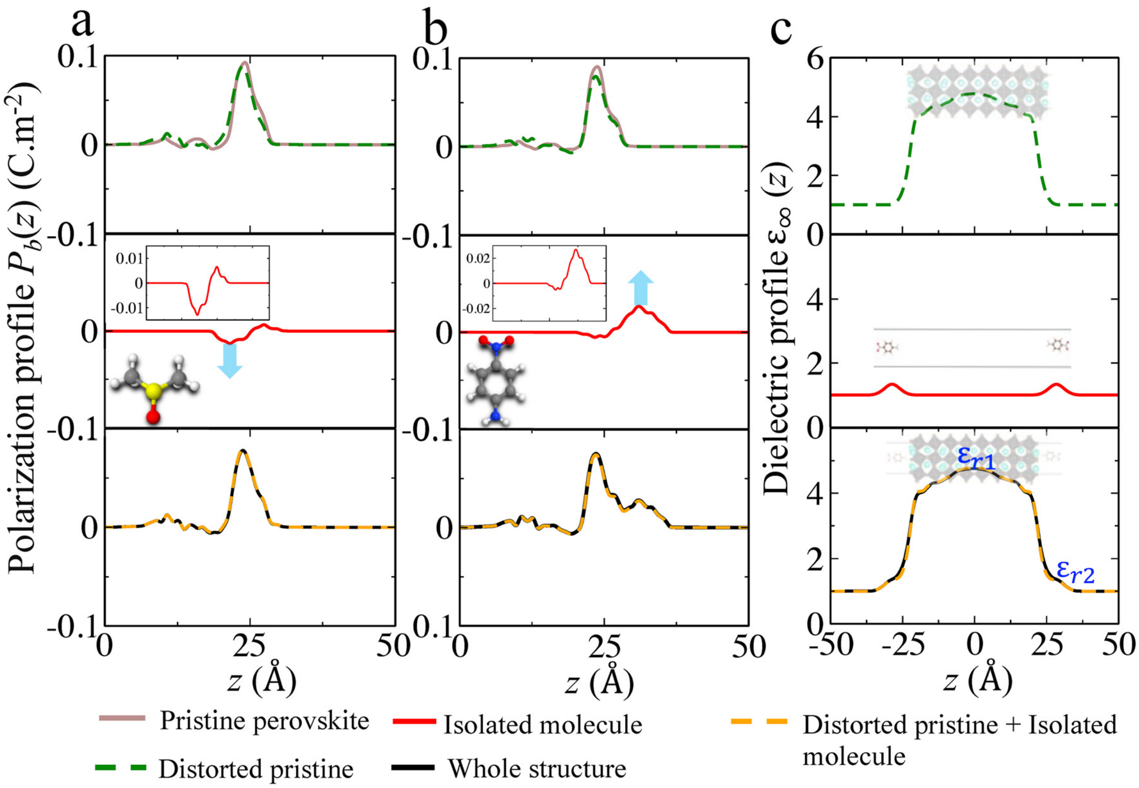

Fig. 5 Additivity of surface dipoles densities illustrated with the plot of the polarization density profiles ($P_b(z)$) computed for (a) DMSO and (b) aniline $-NO_2$ ligands on a CsBr terminated $CsPbBr_3$ surface. A zoom view is shown as inset for isolated molecules. Additivity of electric susceptibilities illustrated with the plot of the position dependent high frequency dielectric profiles ($\varepsilon_\infty(z)$) computed for (c) aniline $-NO_2$ ligand on a CsBr terminated $CsPbBr_3$ surface. Here, the $-NH_2$ group of aniline $-NO_2$ is pointing towards the surface.

individual counterparts (top and middle panel), using the following equation:[67]

$$\varepsilon_\infty^{\text{whole structure}}(z) = \varepsilon_\infty^{\text{pristine distorted}}(z) + \varepsilon_\infty^{\text{isolated molecule}}(z) - 1 \quad (10)$$

demonstrating the additivity of the electric susceptibilities. The position dependent high frequency dielectric profiles of the molecules investigated in the present work are given in ESI (Fig. S21†), with the values lying between 1–1.5.

Revisiting the classical capacitor model for molecular functionalization of halide perovskite surfaces

We end up by revisiting the conventional classical approach based on a capacitor model.[19,68,69] This approach has been widely used in the context of deposition of molecules on Au metal surfaces[70] or TiO_2 surfaces.[71,72] Within this model, the work function at the surface is modulated by $-e\Delta V$, so that $\Delta\phi = -e\Delta V$. The expression for $\Delta\phi$ is computed from the Poisson's equation, given by:

$$\Delta\phi = -e\frac{N_s\mu\cos\theta}{\varepsilon_r\varepsilon_0} \quad (11)$$

where N_s, μ, θ, ε_r and ε_0 are number of dipoles per unit area, dipole moment, tilt angle between dipole and surface normal (see Fig. S3(a)†), dielectric constant and permittivity of free space, respectively. Eqn (11) gives an attractive description of the effect of molecular dipoles on the device properties, including molecular orientation and surface coverage. However, this formula depends on the arbitrary choice of the dielectric permittivity, as already reported for the case of monolayers at water–air interface.[68] Two possible values of ε_r can be reasonably considered: (i) ε_{r1} of perovskite material, and (ii) the effective dielectric constant ε_{r2} at the position of the molecules (Fig. 5(c) and ESI, Fig. S20†). Combining DFT computed dipole moment values (μ) of the isolated free molecules from Table 1, with dipole moment orientations extracted from the optimized functionalized surfaces and $\Delta\phi$ ($\Delta\phi = -\Delta E_v^{abs}$) derived from the Hartree potential approach, we obtain the effective dielectric constants ε_r reported in Table 4. It appears that the dielectric constant at the position of the molecules is closest to the effective dielectric constant needed for an approximate capacitor model. Still, differences between ε_{r2} and ε_r are sizeable. In addition, the dipole orientation also significantly deviates from the ideal situation where $\theta = 0$. Therefore, our semi-classical approach allows recovering the trends already captured by a simple capacitor model but

Table 4 Effective dielectric constant (ε_r) computed using eqn (11). $\Delta\phi$ is the change in work function ($\Delta\phi = -\Delta E_v^{abs}$) computed using the Hartree potential approach. μ is the dipole moment value computed from DFT calculations (Table 1). θ is the tilt angle between the dipole and the surface normal. ε_{r1} and ε_{r2} are the dielectric constant of perovskite materials, and the effective dielectric constant at the position of the molecules (Fig. S21†), respectively

Molecules	$\Delta\phi = -\Delta E_v^{abs}$	μ (D)	θ (°)	$\mu\cos\theta$ (D)	$\varepsilon_r = \frac{-eN\mu\cos\theta}{\varepsilon_0\Delta\phi}$	ε_{r1}	ε_{r2}
Pentylphosphonic acid (phosphonate)	−0.14	1.40	8.20	1.38	2.53	4.7	1.19
Pentanoic acid (oleate)	−0.24	1.59	20.69	1.49	1.59	4.7	1.15
DMSO	−0.35	3.79	52	2.33	1.71	4.7	1.12
Aniline	+0.40	1.70	171.96	−1.68	1.08	4.7	1.22
Aniline –OCH_3	+0.23	1.61	174.49	−1.60	1.78	4.7	1.27
Aniline –NO_2	+1.61	7.44	173.76	−7.39	1.18	4.7	1.32

further provides atomistic information at the interface, with atomistic insight on the interplay between surface dipoles, surface relaxation and charge transfer that directly affects the work function.

Conclusions

In summary, we present a methodology that links the change in surface dipole density to the work function using the classical Maxwell's equation and the output from first-principles calculations. Using $CsPbBr_3$ slabs, we illustrate how surface functionalization *via* tuning the dipole and geometry of ligands effectively controls the work function, with information down to the atomic level. The valence level shifts can be rationalized based on the detailed knowledge of surface dipoles, surface dipole densities, charge transfer as well as local strain effects at the interface as a result of surface–ligand interaction. We observe a continuous decrease in the surface dipole densities correlated with upwards shift of the valence level for DMSO, oleate and phosphonate ligands. A similar behavior is observed for primary, secondary and quaternary alkylammonium ligands, with comparable small changes for all three. Influence of chemical engineering of the surface is further illustrated considering aniline/anilinium and their nitro and methoxy derivatives. Our approach predicts a downward shift of the valence levels that is not experimentally observed, highlighting the limitations of the considered defect and dopant-free surface models. Comparison of results obtained within the present framework with those predicted from the classical capacitor model exemplifies the rather arbitrary choice needed for the effective dielectric constant needed in the later. Overall, our computational strategy provides a useful approach to design and fine tune the energetics of surfaces and interfaces for optimized optoelectronic devices, well beyond the specific case of metal halide perovskites.

Computational details

DFT calculations are performed on basis set of finite-range of numerical atomic orbitals implemented in SIESTA code.[73,74] We use van der Waals density functional with C09 exchange[75] within the van derWaals DF2 flavor to describe the exchange–correlation term for optimizing the atomic positions of the structures. We use a modified version of the SIESTA software "master-post-4.1-251" to include DF2 flavor. This tuning has been suggested to improveC09 based geometry optimization over that with the original DF1 flavor.[76] The structures are fully relaxed using the fast inertial relaxation engine (FIRE) algorithm[77] until the structure satisfies the following relaxation criteria (i) the two consecutive ionic steps have an energy difference less than 10^{-4} eV, and (ii) the maximum forces acting on each atom are less than 0.02 eV Å^{-1}. The single point calculations are performed using the generalized gradient approximation[78] (GGA with PBE) functional including spin–orbit coupling[79] on top of vdwDF2-C09 optimized structures. To correct the band gaps, Slater half occupation technique,[80–82] known as DFT-$\frac{1}{2}$ *i.e.* PBE-$\frac{1}{2}$ is used (see ESI, section I.3†). We take a polarized double-zeta basis set with an energy shift of 50 meV for bulk $CsPbBr_3$. To describe accurately the properties of the surfaces, we include orbitals with weight in the vacuum region, known as diffuse orbitals:[83] diffuse orbitals (5s, 5p, 5d) for Br atom on the top of two atomic layers on both sides of the slab with 30% diffuse orbital size or cutoff radii. A real space mesh grid energy cutoff of 350 Ry is used for our calculations. For the high-frequency dielectric constant profiles calculations, an electric field of 0.025 eV Å^{-1} is applied along the [001] direction. A detailed discussion for the computational details is given in ESI, section I.† Note that, to reduce the computational burden, we consider a converged five carbons chain length for oleate and phosphonate (see section IV of the ESI for details†).

Conflicts of interest

There are no conflicts to declare.

Acknowledgements

Authors acknowledge funding from the European Union's Horizon 2020 program, through an Innovation Action under Grant Agreement No. 861985 (PeroCUBE) and through a FET Open research and innovation action under the Grant Agreement No. 899141 (PoLLoC). J. E. acknowledges the financial support from the Institut Universitaire de France. This work was granted access to the HPC resources of TGCC under the allocations 2021-A0110907682 and 2022-A0110907682 made by GENCI. Authors are grateful to Maksym Kovalenko and Andriy Stelmakh for useful discussions and providing the MD snapshots.

References

1 A. Kojima, K. Teshima, Y. Shirai and T. Miyasaka, Organometal halide perovskites as visible-light sensitizers for photovoltaic cells, *J. Am. Chem. Soc.*, 2009, **131**, 6050–6051.

2 R. J. Sutton, G. E. Eperon, L. Miranda, E. S. Parrott, B. A. Kamino, J. B. Patel, M. T. Hörantner, M. B. Johnston, A. A. Haghighirad, D. T. Moore, *et al.*, Bandgap-tunable cesium lead halide perovskites with high thermal stability for efficient solar cells, *Adv. Energy Mater.*, 2016, **6**, 1502458.

3 G. R. Yettapu, D. Talukdar, S. Sarkar, A. Swarnkar, A. Nag, P. Ghosh and P. Mandal, Terahertz conductivity within colloidal $CsPbBr_3$ perovskite nanocrystals: remarkably high carrier mobilities and large diffusion lengths, *Nano Lett.*, 2016, **16**, 4838–4848.

4 J. H. Heo, S. H. Im, J. H. Noh, T. N. Mandal, C.-S. Lim, J. A. Chang, Y. H. Lee, H.-j. Kim, A. Sarkar, M. K. Nazeeruddin, *et al.*, Efficient inorganic–organic hybrid heterojunction solar cells containing perovskite compound and polymeric hole conductors, *Nat. Photonics*, 2013, **7**, 486–491.

5 J. Kang and L.-W. Wang, High defect tolerance in lead halide perovskite $CsPbBr_3$, *J. Phys. Chem. Lett.*, 2017, **8**, 489–493.

6 W. S. Yang, B.-W. Park, E. H. Jung, N. J. Jeon, Y. C. Kim, D. U. Lee, S. S. Shin, J. Seo, E. K. Kim, J. H. Noh, *et al.*, Iodide management in formamidinium-lead-halide–based perovskite layers for efficient solar cells, *Science*, 2017, **356**, 1376–1379.

7 L. Dou, Y. M. Yang, J. You, Z. Hong, W.-H. Chang, G. Li and Y. Yang, Solution-processed hybrid perovskite photodetectors with high detectivity, *Nat. Commun.*, 2014, **5**, 1–6.

8 H. Cho, S.-H. Jeong, M.-H. Park, Y.-H. Kim, C. Wolf, C.-L. Lee, J. H. Heo, A. Sadhanala, N. Myoung, S. Yoo, *et al.*, Overcoming the electroluminescence efficiency limitations of perovskite light-emitting diodes, *Science*, 2015, **350**, 1222–1225.

9 G. Xing, N. Mathews, S. S. Lim, N. Yantara, X. Liu, D. Sabba, M. Grätzel, S. Mhaisalkar and T. C. Sum, Low-temperature solution-processed wavelength-tunable perovskites for lasing, *Nat. Mater.*, 2014, **13**, 476–480.

10 P. Schulz, D. Cahen and A. Kahn, Halide perovskites: is it all about the interfaces?, *Chem. Rev.*, 2019, **119**, 3349–3417.

11 B. Wang, H. Li, Q. Dai, M. Zhang, Z. Zou, J.-L. Brédas and Z. Lin, Robust Molecular Dipole-Enabled Defect Passivation and Control of Energy-Level Alignment for High-Efficiency Perovskite Solar Cells, *Angew. Chem.*, 2021, **133**, 17805–17811.

12 H. J. Lee, A. C. Jamison and T. R. Lee, Surface dipoles: a growing body of evidence supports their impact and importance, *Acc. Chem. Res.*, 2015, **48**, 3007–3015.

13 L. Canil, T. Cramer, B. Fraboni, D. Ricciarelli, D. Meggiolaro, A. Singh, M. Liu, M. Rusu, C. M. Wolff, N. Phung, *et al.*, Tuning halide perovskite energy levels, *Energy Environ. Sci.*, 2021, **14**, 1429–1438.

14 K.-G. Lim, S. Ahn and T.-W. Lee, Energy level alignment of dipolar interface layer in organic and hybrid perovskite solar cells, *J. Mater. Chem. C*, 2018, **6**, 2915–2924.

15 W. Kong, W. Li, C. Liu, H. Liu, J. Miao, W. Wang, S. Chen, M. Hu, D. Li, A. Amini, *et al.*, Organic monomolecular layers enable energy-level matching for efficient hole transporting layer free inverted perovskite solar cells, *ACS Nano*, 2019, **13**, 1625–1634.

16 K. Hills-Kimball, H. Yang, T. Cai, J. Wang and O. Chen, Recent Advances in Ligand Design and Engineering in Lead Halide Perovskite Nanocrystals, *Adv. Sci.*, 2021, 2100214.

17 W. Melitz, J. Shen, A. C. Kummel and S. Lee, Kelvin probe force microscopy and its application, *Surf. Sci. Rep.*, 2011, **66**, 1–27.

18 I. D. Baikie, A. C. Grain, J. Sutherland and J. Law, Ambient pressure photoemission spectroscopy of metal surfaces, *Appl. Surf. Sci.*, 2014, **323**, 45–53.

19 R. J. Demchak and T. Fort Jr., Surface, Dipole moments of close-packed un-ionized monolayers at the air-water interface, *J. Colloid Interface Sci.*, 1974, **46**, 191–202.

20 T. Leung, C. Kao, W. Su, Y. Feng and C. Chan, Relationship between surface dipole, work function and charge transfer: Some exceptions to an established rule, *Phys. Rev. B: Condens. Matter Mater. Phys.*, 2003, **68**, 195408.

21 Y. Zheng, Z. Fang, M. Shang, Q. Sun, J. Zheng, Z. Yang, X. Hou and W. Yang, Linearly Tailored Work Function of Orthorhombic $CsSnI_3$ Perovskites, *ACS Energy Lett.*, 2021, **6**, 2328–2335.

22 B. Traoré, P. Basera, A. J. Ramadan, H. J. Snaith, C. Katan and J. Even, A Theoretical Framework for Microscopic Surface and Interface Dipoles, Work Functions, and Valence Band Alignments in 2D and 3D Halide Perovskite Heterostructures, *ACS Energy Lett.*, 2021, **7**, 349–357.

23 J. Zheng, J. Chen, D. Ouyang, Z. Huang, X. He, J. Kim and W. C. Choy, Critical Role of Functional Groups in Defect Passivation and Energy Band Modulation in Efficient and Stable Inverted Perovskite Solar Cells Exceeding 21% Efficiency, *ACS Appl. Mater. Interfaces*, 2020, **12**, 57165–57173.

24 J. Duan, M. Wang, Y. Wang, J. Zhang, Q. Guo, Q. Zhang, Y. Duan and Q. Tang, Effect of Side-Group-Regulated Dipolar Passivating Molecules on $CsPbBr_3$ Perovskite Solar Cells, *ACS Energy Lett.*, 2021, **6**, 2336–2342.

25 J. Pan, H. Huang, W. Zhao, D. Lin, Z. Nie, J. Zhong, L. Ma and X. Zhang, Efficient and Stable Self-Assembly Blue-

Emitting $CsPbBr_3$ Nanoplatelets with Self-Repaired Surface Defects, *ACS Appl. Nano Mater.*, 2022, **5**, 15062–15069.

26 G. Rainò, G. Nedelcu, L. Protesescu, M. I. Bodnarchuk, M. V. Kovalenko, R. F. Mahrt and T. Stöferle, Single cesium lead halide perovskite nanocrystals at low temperature: fast single-photon emission, reduced blinking, and exciton fine structure, *ACS Nano*, 2016, **10**, 2485–2490.

27 C. C. Stoumpos, C. D. Malliakas, J. A. Peters, Z. Liu, M. Sebastian, J. Im, T. C. Chasapis, A. C. Wibowo, D. Y. Chung, A. J. Freeman, *et al.*, Crystal growth of the perovskite semiconductor $CsPbBr_3$: a new material for high-energy radiation detection, *Cryst. Growth Des.*, 2013, **13**, 2722–2727.

28 J. Peng, C. Q. Xia, Y. Xu, R. Li, L. Cui, J. K. Clegg, L. M. Herz, M. B. Johnston and Q. Lin, Crystallization of $CsPbBr_3$ single crystals in water for X-ray detection, *Nat. Commun.*, 2021, **12**, 1–10.

29 D. N. Dirin, I. Cherniukh, S. Yakunin, Y. Shynkarenko and M. V. Kovalenko, Solution-grown $CsPbBr_3$ perovskite single crystals for photon detection, *Chem. Mater.*, 2016, **28**, 8470–8474.

30 Y. Rakita, N. Kedem, S. Gupta, A. Sadhanala, V. Kalchenko, M. L. Böhm, M. Kulbak, R. H. Friend, D. Cahen and G. Hodes, Low-temperature solution-grown $CsPbBr_3$ single crystals and their characterization, *Cryst. Growth Des.*, 2016, **16**, 5717–5725.

31 R. Chen, Z. Liang, W. Feng, X. Hu and A. Hao, Solution-processed all-inorganic perovskite $CsPbBr_3$ thin films for optoelectronic application, *J. Alloys Compd.*, 2021, **864**, 158125.

32 Q. A. Akkerman, S. G. Motti, A. R. Srimath Kandada, E. Mosconi, V. DâInnocenzo, G. Bertoni, S. Marras, B. A. Kamino, L. Miranda, F. De Angelis, *et al.*, Solution synthesis approach to colloidal cesium lead halide perovskite nanoplatelets with monolayer-level thickness control, *J. Am. Chem. Soc.*, 2016, **138**, 1010–1016.

33 G. Rainò, N. Yazdani, S. C. Boehme, M. Kober-Czerny, C. Zhu, F. Krieg, M. D. Rossell, R. Erni, V. Wood, I. Infante, *et al.*, Ultra-narrow room-temperature emission from single $CsPbBr_3$ perovskite quantum dots, *Nat. Commun.*, 2022, **13**, 1–8.

34 I. Cherniukh, G. Rainò, T. Stöferle, M. Burian, A. Travesset, D. Naumenko, H. Amenitsch, R. Erni, R. F. Mahrt, M. I. Bodnarchuk, *et al.*, Perovskite-type superlattices from lead halide perovskite nanocubes, *Nature*, 2021, **593**, 535–542.

35 G. Rainò, M. A. Becker, M. I. Bodnarchuk, R. F. Mahrt, M. V. Kovalenko and T. Stöferle, Superfluorescence from lead halide perovskite quantum dot superlattices, *Nature*, 2018, **563**, 671–675.

36 A. A. Petrov, S. A. Fateev, V. N. Khrustalev, Y. Li, P. V. Dorovatovskii, Y. V. Zubavichus, E. A. Goodilin and A. B. Tarasov, Formamidinium haloplumbate intermediates: the missing link in a chain of hybrid perovskites crystallization, *Chem. Mater.*, 2020, **32**, 7739–7745.

37 G. Nedelcu, L. Protesescu, S. Yakunin, M. I. Bodnarchuk, M. J. Grotevent and M. V. Kovalenko, Fast anion-exchange in highly luminescent nanocrystals of cesium lead halide perovskites (CsPbX3, X = Cl, Br, I), *Nano Lett.*, 2015, **15**, 5635–5640.

38 J. De Roo, M. Ibáñez, P. Geiregat, G. Nedelcu, W. Walravens, J. Maes, J. C. Martins, I. Van Driessche, M. V. Kovalenko and Z. Hens, Highly dynamic ligand binding and light absorption coefficient of cesium lead bromide perovskite nanocrystals, *ACS Nano*, 2016, **10**, 2071–2081.

39 W.-k. Koh, S. Park and Y. Ham, Phosphonic acid stabilized colloidal CsPbX3 (X = Br, I) perovskite nanocrystals and their surface chemistry, *ChemistrySelect*, 2016, **1**, 3479–3482.

40 M. Imran, P. Ijaz, L. Goldoni, D. Maggioni, U. Petralanda, M. Prato, G. Almeida, I. Infante and L. Manna, Simultaneous cationic and anionic ligand exchange for colloidally stable $CsPbBr_3$ nanocrystals, *ACS Energy Lett.*, 2019, **4**, 819–824.

41 A. Franciosi and C. G. Van de Walle, Heterojunction band offset engineering, *Surf. Sci. Rep.*, 1996, **25**, 1–140.

42 A. Stelmakh, M. Aebli, A. Baumketner and M. V. Kovalenko, On the mechanism of alkylammonium ligands binding to the surface of $CsPbBr_3$ nanocrystals, *Chem. Mater.*, 2021, **33**, 5962–5973.

43 C. Schmitt, Surface modification of oxide nanoparticles using phosphonic acids: characterization, surface dynamics, and dispersion in sols and nanocomposites, Ph. D. thesis, Université Montpellier, 2015.

44 E. Mognaschi, L. Zullino and A. Chierico, Associating behaviour of pure polar liquids: dielectric properties of n-valeric acid, *J. Phys. D: Appl. Phys.*, 1984, **17**, 1007.

45 D. R. Lide, *CRC handbook of chemistry and physics*, CRC press, 2004, vol. 85.

46 S. Itoh and H. Ohtaki, A study of the liquid structure of dimethyl sulfoxide by the X-ray diffraction, *Z. Naturforsch., A: Phys. Sci.*, 1987, **42**, 858–862.

47 H. Yoneda, Effect of substitution on dipole moments of molecules, *Bull. Chem. Soc. Jpn.*, 1958, **31**, 708–714.

48 M. I. Bodnarchuk, S. C. Boehme, S. ten Brinck, C. Bernasconi, Y. Shynkarenko, F. Krieg, R. Widmer, B. Aeschlimann, D. Günther, M. V. Kovalenko, *et al.*, Rationalizing and controlling the surface structure and electronic passivation of cesium lead halide nanocrystals, *ACS Energy Lett.*, 2018, **4**, 63–74.

49 L. Protesescu, S. Yakunin, M. I. Bodnarchuk, F. Krieg, R. Caputo, C. H. Hendon, R. X. Yang, A. Walsh and M. V. Kovalenko, Nanocrystals of cesium lead halide perovskites ($CsPbX_3$, X = Cl, Br, and I): novel optoelectronic materials showing bright emission with wide color gamut, *Nano Lett.*, 2015, **15**, 3692–3696.

50 D. P. Nenon, K. Pressler, J. Kang, B. A. Koscher, J. H. Olshansky, W. T. Osowiecki, M. A. Koc, L.-W. Wang and A. P. Alivisatos, Design principles for trap-free $CsPbX_3$ nanocrystals: enumerating and eliminating surface halide vacancies with softer Lewis bases, *J. Am. Chem. Soc.*, 2018, **140**, 17760–17772.

51 B. Zhang, L. Goldoni, J. Zito, Z. Dang, G. Almeida, F. Zaccaria, J. De Wit, I. Infante, L. De Trizio and L. Manna, Alkyl phosphonic acids deliver $CsPbBr_3$ nanocrystals with high photoluminescence quantum yield and truncated octahedron shape, *Chem. Mater.*, 2019, **31**, 9140–9147.

52 G. Almeida, O. J. Ashton, L. Goldoni, D. Maggioni, U. Petralanda, N. Mishra, Q. A. Akkerman, I. Infante, H. J. Snaith and L. Manna, The phosphine oxide route toward lead halide perovskite nanocrystals, *J. Am. Chem. Soc.*, 2018, **140**, 14878–14886.

53 J. Y. Woo, S. Lee, S. Lee, W. D. Kim, K. Lee, K. Kim, H. J. An, D. C. Lee and S. Jeong, Air-stable PbSe nanocrystals passivated by phosphonic acids, *J. Am. Chem. Soc.*, 2016, **138**, 876–883.

54 J. Shamsi, D. Kubicki, M. Anaya, Y. Liu, K. Ji, K. Frohna, C. P. Grey, R. H. Friend and S. D. Stranks, Stable hexylphosphonate-capped blue-emitting quantum-confined $CsPbBr_3$ nanoplatelets, *ACS Energy Lett.*, 2020, **5**, 1900–1907.

55 L. Pedesseau, D. Sapori, B. Traore, R. Robles, H.-H. Fang, M. A. Loi, H. Tsai, W. Nie, J.-C. Blancon, A. Neukirch, *et al.*, Advances and promises of layered halide hybrid perovskite semiconductors, *ACS Nano*, 2016, **10**, 9776–9786.

56 J. L. Knutson, J. D. Martin and D. B. Mitzi, Tuning the band gap in hybrid tin iodide perovskite semiconductors using structural templating, *Inorg. Chem.*, 2005, **44**, 4699–4705.

57 J. Even, L. Pedesseau, J.-M. Jancu and C. Katan, Importance of spin–orbit coupling in hybrid organic/inorganic perovskites for photovoltaic applications, *J. Phys. Chem. Lett.*, 2013, **4**, 2999–3005.

58 L. Hu, C. Wang, R. M. Kennedy, L. D. Marks and K. R. Poeppelmeier, The role of oleic acid: From synthesis to assembly of perovskite nanocuboid two-dimensional arrays, *Inorg. Chem.*, 2015, **54**, 740–745.

59 N. Ahn, D.-Y. Son, I.-H. Jang, S. M. Kang, M. Choi and N.-G. Park, Highly reproducible perovskite solar cells with average efficiency of 18.3% and best efficiency of 19.7% fabricated via Lewis base adduct of lead(II) iodide, *J. Am. Chem. Soc.*, 2015, **137**, 8696–8699.

60 R. Vidal, J.-A. Alberola-Borràs, S. N. Habisreutinger, J.-L. Gimeno-Molina, D. T. Moore, T. H. Schloemer, I. Mora-Seró, J. J. Berry and J. M. Luther, Assessing health and environmental impacts of solvents for producing perovskite solar cells, *Nat. Sustain.*, 2021, **4**, 277–285.

61 Y. Shynkarenko, M. I. Bodnarchuk, C. Bernasconi, Y. Berezovska, V. Verteletskyi, S. T. Ochsenbein and M. V. Kovalenko, Direct synthesis of quaternary alkylammonium-capped perovskite nanocrystals for efficient blue and green light-emitting diodes, *ACS Energy Lett.*, 2019, **4**, 2703–2711.

62 J. Pan, L. N. Quan, Y. Zhao, W. Peng, B. Murali, S. P. Sarmah, M. Yuan, L. Sinatra, N. M. Alyami, J. Liu, *et al.*, Highly efficient perovskite-quantum-dot light-emitting diodes by surface engineering, *Adv. Mater.*, 2016, **28**, 8718–8725.

63 Y. Chen, S. R. Smock, A. H. Flintgruber, F. A. Perras, R. L. Brutchey and A. J. Rossini, Surface termination of $CsPbBr_3$ perovskite quantum dots determined by solid-state NMR spectroscopy, *J. Am. Chem. Soc.*, 2020, **142**, 6117–6127.

64 F. Giustino and A. Pasquarello, Theory of atomic-scale dielectric permittivity at insulator interfaces, *Phys. Rev. B: Condens. Matter Mater. Phys.*, 2005, **71**, 144104.

65 N. Shi and R. Ramprasad, Atomic-scale dielectric permittivity profiles in slabs and multilayers, *Phys. Rev. B: Condens. Matter Mater. Phys.*, 2006, **74**, 045318.

66 D. Sapori, M. Kepenekian, L. Pedesseau, C. Katan and J. Even, Quantum confinement and dielectric profiles of colloidal nanoplatelets of halide inorganic and hybrid organic–inorganic perovskites, *Nanoscale*, 2016, **8**, 6369–6378.

67 B. Traore, L. Pedesseau, L. Assam, X. Che, J.-C. Blancon, H. Tsai, W. Nie, C. C. Stoumpos, M. G. Kanatzidis, S. Tretiak, *et al.*, Composite nature of layered hybrid perovskites: assessment on quantum and dielectric confinements and band alignment, *ACS Nano*, 2018, **12**, 3321–3332.

68 O. N. Oliveira, D. M. Taylor, T. J. Lewis, S. Salvagno and C. J. Stirling, Estimation of group dipole moments from surface potential measurements on Langmuir monolayers, *J. Chem. Soc., Faraday Trans. 1*, 1989, **85**, 1009–1018.

69 J. Davies and S. E. Rideal, Interfacial potentials, *Can. J. Chem.*, 1955, **33**, 947–960.

70 P. C. Rusu and G. Brocks, Surface dipoles and work functions of alkylthiolates and fluorinated alkylthiolates on Au (111), *J. Phys. Chem. B*, 2006, **110**, 22628–22634.

71 C. Goh, S. R. Scully and M. D. McGehee, Effects of molecular interface modification in hybrid organic-inorganic photovoltaic cells, *J. Appl. Phys.*, 2007, **101**, 114503.

72 T. Zhu, J. Su, J. Alvarez, G. Lefèvre, F. Labat, I. Ciofini and T. Pauporté, Response Enhancement of Self-Powered Visible-Blind UV Photodetectors by Nanostructured Heterointerface Engineering, *Adv. Funct. Mater.*, 2019, **29**, 1903981.

73 E. Artacho, E. Anglada, O. Diéguez, J. D. Gale, A. García, J. Junquera, R. M. Martin, P. Ordejón, J. M. Pruneda, D. Sánchez-Portal, *et al.*, The SIESTA method; developments and applicability, *J. Phys.: Condens. Matter*, 2008, **20**, 064208.

74 J. M. Soler, E. Artacho, J. D. Gale, A. García, J. Junquera, P. Ordejón and D. Sánchez-Portal, The SIESTA method for ab initio order-N materials simulation, *J. Phys.: Condens. Matter*, 2002, **14**, 2745.

75 V. R. Cooper, van der Waals density functional: An appropriate exchange functional, *Phys. Rev. B: Condens. Matter Mater. Phys.*, 2010, **81**, 161104.

76 I. Hamada and M. Otani, Comparative van der Waals density-functional study of graphene on metal surfaces, *Phys. Rev. B: Condens. Matter Mater. Phys.*, 2010, **82**, 153412.

77 E. Bitzek, P. Koskinen, F. Gähler, M. Moseler and P. Gumbsch, Structural relaxation made simple, *Phys. Rev. Lett.*, 2006, **97**, 170201.

78 J. P. Perdew, K. Burke and M. Ernzerhof, Generalized gradient approximation made simple, *Phys. Rev. Lett.*, 1996, **77**, 3865.

79 L. Fernández-Seivane, M. A. Oliveira, S. Sanvito and J. Ferrer, On-site approximation for spin–orbit coupling in linear combination of atomic orbitals density functional methods, *J. Phys.: Condens. Matter*, 2006, **18**, 7999.

80 L. G. Ferreira, M. Marques and L. K. Teles, Approximation to density functional theory for the calculation of band gaps of semiconductors, *Phys. Rev. B: Condens. Matter Mater. Phys.*, 2008, **78**, 125116.

81 S. X. Tao, X. Cao and P. A. Bobbert, Accurate and efficient band gap predictions of metal halide perovskites using the DFT-1/2 method: GW accuracy with DFT expense, *Sci. Rep.*, 2017, **7**, 1–9.

82 B. Traoré, J. Even, L. Pedesseau, M. Kepenekian and C. Katan, Band gap, effective masses, and energy level alignment of 2D and 3D halide perovskites and heterostructures using DFT-1/2, *Phys. Rev. Mater.*, 2022, **6**, 014604.

83 S. García-Gil, A. García, N. Lorente and P. Ordejón, Optimal strictly localized basis sets for noble metal surfaces, *Phys. Rev. B: Condens. Matter Mater. Phys.*, 2009, **79**, 075441.